Heliyon 9 (2023) e20689

Contents lists available at ScienceDirect

Heliyon

journal homepage: www.cell.com/heliyon

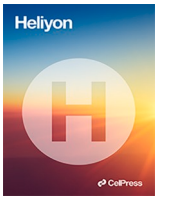

Novel magnetic nanocomposites $BiFeO_3$/Cu(BDC) for efficient dye removal

Fatemeh Shahrab, Azadeh Tadjarodi *

Research Laboratory of Inorganic Materials Synthesis, Department of Chemistry, Iran University of Science and Technology (IUST), 16846-13114, Tehran, Iran

ARTICLE INFO

Keywords:
Bismuth ferrite nanoparticles
Cu(BDC) metal organic framework
Magnetic nanocomposite
Photocatalytic degradation
Electrochemical properties

ABSTRACT

In this study, bismuth ferrite nanoparticles and metal-organic framework, Cu(BDC), were prepared by microwave-assisted combustion in solid state and ultrasound-assisted method, respectively. To enhance the properties of bismuth ferrite nanoparticles and Cu(BDC), we form them as their composite through microwave and ultrasonic probe strategies. Various analyses, including FT-IR, XRD, SEM, DRS, VSM, and so on, were applied to verify the synthesis accuracy. Then, the catalytic performances of the nanoparticles and the as-prepared nanocomposites were evaluated through photocatalytic degradation of methyl orange. Furthermore, the adsorption capacity of the as-synthesized materials was assessed toward the Congo red removal from wastewater. All the results prove that the proposed nanocomposite can be an acceptable candidate for eliminating contaminants from wastewater. The electrochemical properties of bismuth ferrite, $BiFeO_3$/Cu (BDC) nanocomposite 1, and $BiFeO_3$/Cu(BDC) nanocomposite 2 have been studied by cyclic voltammetry.

1. Introduction

Recently, industrial discharge of organic dye molecules has emerged as a prominent contributor to environmental contamination among the myriad of wastewater pollutants. Sectors such as textile, paper, and rubber manufacturing generate substantial volumes of these pollutants, characterized by their toxicity, non-biodegradability, and detrimental effects on human health and environmental sustainability. Additionally, these pollutants have been identified as carcinogenic agents, exacerbating their hazardous nature [1–3]. Addressing the escalating environmental concerns, research groups have increasingly focused on investigating methods to dissolve and mitigate the presence of visually vivid dyes in wastewater. This pursuit stems from the imperative to meet growing environmental standards and necessitates the development of effective treatments for such wastewater [4–8]. A range of heterogeneous physical and chemical mechanisms have been employed to eradicate dyes from wastewater. These strategies encompass diverse approaches, including precipitation, air stripping, adsorption, reverse osmosis, flocculation, and ultrafiltration. Each method has been harnessed to target the efficient and comprehensive removal of dyes from their corresponding wastewater matrices [9–17].

Advancements in science and technology have paved the way for the utilization of photocatalytic degradation as a viable mechanism for removing dye molecules from polluted water sources. Notably, the utilization of solar energy as a clean and renewable energy source has garnered significant attention for its potential application in addressing environmental concerns. Consequently, the exploration and investigation of solar energy exploitation for environmental purposes have become subjects of widespread research on

* Corresponding author.
E-mail addresses: f.shahrab@yahoo.com (F. Shahrab), tajarodi@iust.ac.ir (A. Tadjarodi).

https://doi.org/10.1016/j.heliyon.2023.e20689
Received 1 May 2023; Received in revised form 9 August 2023; Accepted 4 October 2023
Available online 21 October 2023

a global scale [18–22]. Photocatalysis, entails the simultaneous occurrence of oxidation and reduction reactions on the surface of a solid photocatalyst. These reactions are facilitated by generating of photogenerated charge carriers, such as holes and electrons, which emerge as a consequence of light absorption by the photocatalyst material [23–28]. Due to the paramount importance of quantum yield and solar energy conversion efficiency in achieving enhanced photocatalytic activity, extensive research efforts have been dedicated to exploring and optimizing the properties of bismuth-based compounds [29–31].

The utilization of bimetallic nanoparticles, resulting from the synergistic interaction between two distinct metals, has emerged as a promising avenue for enhancing and tailoring their inherent characteristics. This combination engenders novel and versatile properties, augmenting their efficacy in diverse fields, including electrochemistry, catalysis, and optics. In particular, bimetallic nanoparticles have garnered considerable attention as catalysts for various chemical reactions, exemplified by the oxidation, reduction, and degradation of various compounds, including dyes. Such applications have yielded substantial advancements in these domains, further underscoring the significance and potential of bimetallic nanoparticles in scientific research and technological innovation [32–34]. Multiferroic materials exhibit the intriguing property of simultaneously manifesting ferroelectricity, ferromagnetism, or ferroelasticity within a single material. This distinctive characteristic arises from the robust coupling of electric, magnetic, and structural order parameters. Consequently, multiferroic materials offer diverse opportunities for various applications, including information storage, spintronic devices, magnetic recording media, and sensors. The unique combination of multipleferroic properties within a single material holds tremendous potential for enabling novel functionalities and advancing technological advancements in various fields [35–38]. Bismuth Ferrite ($BiFeO_3$) has gained significant prominence as a widely studied multiferroic material due to its remarkable coexistence of magnetic and electric ordering, exhibiting ferroelectric and anti-ferromagnetic (AFM) characteristics. Moreover, $BiFeO_3$ possesses a relatively narrow band gap and shows the bulk photovoltaic effect, rendering it particularly intriguing for solar energy-related applications. Consequently, the unique properties of $BiFeO_3$ make it a compelling candidate as a photocatalyst for organic pollutant degradation. The distinctive combination of multiferroic behavior, favorable band gap, and photovoltaic effect endows $BiFeO_3$ with remarkable potential for advanced photocatalytic systems. Extensive research efforts dedicated to exploring and harnessing the diverse functionalities of $BiFeO_3$-based materials for efficient and sustainable photocatalysis [39–44]. In 2018, a suite of cobalt ferrite nanostructures doped with bismuth ($CoBixFe_{2-x}O_4$, x = 0.02, 0.04, 0.06, 0.08, 0.1) were synthesized via the sol-gel approach to investigate their catalytic efficiency in the degradation of harmful dyes under both visible light irradiation and non-irradiated conditions [45,46]. The authors postulated that the success of materials in catalytic processes can be attributed to factors such as crystallite size, saturation magnetization, and band gap. Additionally, the efficient removal of hazardous dyes by the synthesized samples highlighted their potential as catalysts. Recently, Ruby et al. conducted a study on Bismuth ferrite heterostructures composed of interconnected nanosheets (BHNs) to evaluate their photocatalytic capabilities in the degradation of methyl orange under sunlight irradiation. The photocatalytic experiments demonstrated a significant ~86 % degradation of methyl orange for 150 min. Consequently, they asserted that the photocatalytic activity of BHNs makes them exceptional candidates for the degradation of various organic pollutants under sunlight irradiation [47].

In contaminant elimination, adsorption is widely acknowledged as a highly viable approach due to its exceptional efficacy, minimal generation of by-products, relatively economical nature, and straightforward operational procedures. Diverse porous materials, encompassing activated carbons, clay and modified clay, cellulosic derivatives, zeolites, and polymer-based substances, have effectively been employed to treat various types of pollutants. Porous materials are solid matrices characterized by empty interstitial spaces capable of accommodating other entities [48–51]. Metal-organic frameworks (MOFs) represent a category of crystalline porous materials that exhibit three-dimensional structures constructed from metal clusters or ions and organic linkers. MOFs demonstrate exceptional attributes, including specific surface areas reaching up to 3000 $m^2\ g^{-1}$ and specific pore volumes of up to 1 g cm^{-3}. These values are among the most exceptional ever documented for other compounds [52–55]. Metal-organic frameworks (MOFs) represent a subset of nanocomposite materials that exhibit remarkable potential in diverse applications such as gas storage, chemical sensing, separation processes, drug delivery systems, and heterogeneous catalysis. The inherent porous structure of MOFs facilitates efficient transportation of reactants and products, enabling their transformation into highly effective heterogeneous catalysts. It is noteworthy that each metal-oxo cluster present within MOFs can be regarded as an individual quantum dot, possessing properties akin to a semiconductor, functioning as a light absorber, charge generator, and catalytic site [56–62]. The utilization of nanomaterials in water treatment represents a pivotal and significant application. These nanoscale structures have exhibited outstanding efficacy in removing of contaminants, particularly in the adsorption of various pollutants, notably azo dyes [63–70].

In this research, $BiFeO_3$ was synthesized utilizing a solid-state microwave-assisted combustion approach. Concurrently, a metal-organic framework (MOF) known as Cu(BDC) was synthesized and subsequently incorporated into $BiFeO_3$, resulting in the creation of innovative composites with synergistic capabilities in terms of adsorption and photocatalytic performance. The photocatalytic degradation efficiency of the prepared materials was assessed by examining their response toward the organic dye methyl orange. Furthermore, the adsorption capacity of the materials toward Congo red was investigated. The comprehensive findings of various characterization analyses will be presented in this study.

2. Experimental section

2.1. Material and methods

All reagents employed in this study were procured from reputable sources, namely Merck and Sigma-Aldrich companies, and were utilized without additional purification steps. Infrared spectra were obtained using a Nicolet Fourier Transform FT-IR, Nicolet 100 spectrometer, within the range of 500–4000 cm-1, employing a KBr tablet. Powder X-ray diffraction (XRD) measurements were

conducted using a Philips X'pert diffractometer equipped with monochromated Cu-kα radiation ($\lambda = 1.54056$ Å). The morphology of the materials was examined using a scanning electron microscope (SEM), specifically the TESCAN VEGA II (Czech). Magnetic characterization was performed using a vibrating sample magnetometer (VSM, 7400, Lakeshore). The UV–vis diffuse reflectance spectra (DRS) were recorded using a UV–Vis spectrometer (UV-2550). Inductively coupled plasma atomic emission spectrometry (ICP-AES) was carried out on a Varian Vista-PRO instrument, equipped with a charge-coupled detector, to determine the residual concentration of Bismuth ions in the composites.

The experimental conditions in the synthesis process significantly impact the properties of the nanoparticles. Parameters, including microwave oven time, power, fuel type, and fuel/oxidant ratio, were systematically investigated to identify the optimum conditions that would yield a substantial nanoparticle yield. A detailed summary of the different pathways explored, along with their corresponding outcomes, is provided in Table 1.

2.2. Preparation of $BiFeO_3$ nanoparticles

For the synthesis of $BiFeO_3$ nanoparticles, a mixture was prepared by combining, 1 mmol (0.485 g) of $Bi(NO_3)_35H_2O$, 1 mmol (0.404 g) $Fe(NO_3)_39H_2O$, 3 mmol glycine (NH_2CH_2COOH) and 6 mmol of ammonium nitrate in a small crucible. Subsequently, the resulting mixture was carefully transferred into another crucible containing CuO powder.

Including copper oxide powder in the crucible serves a crucial purpose in facilitating the reaction process. Copper oxide acts as an efficient absorber of microwave radiation, which is essential for promoting the reaction kinetics. Without copper oxide, the reaction would encounter significant challenges and proceed at a notably slow rate due to the scattering of microwave radiation within the microwave cavity. By incorporating copper oxide powder in the crucible, the concentration of microwave radiation is enhanced, leading to improved reaction efficiency and kinetics. The prepared mixture was introduced into a conventional domestic microwave oven operating at a power level of 360 W for 20 min. Subsequently, the resulting residue was thoroughly washed with distilled water, followed by ethanol, and later dried in an oven set at a temperature of 70 °C. A schematic representation illustrating the synthetic path is presented (Scheme ESI 1). According to the proposed mechanistic pathway, the reaction initiates by forming a coordination intermediate between metal ions and glycine. The subsequent decomposition of the organic moiety within this intermediate generates bismuth and iron oxides, ultimately resulting in the formation of $BiFeO_3$.

1) $Bi)NO_3(_3\cdot\ 5H_2O + Fe)NO_3(_3\cdot\ 9H_2O + NH_2CH_2COOH + 2NH_4NO_3 \rightarrow Bi[Fe(NH_2CH_2COO)](NO_3)_3\cdot H_2O + 7\ NO_2 + 14H_2O + 7/2H_2$
2) $2\ Bi\ [Fe(NH_2CH_2COO)]\ (NO_3)_3\cdot H_2O + 6O_2 \rightarrow Bi_2O_3 + Fe_2O_3 + 8\ NO_2 + 6H_2O + 4CO_2$

Table 1
Effective parameters on synthesis procedure of $BiFeO_3$ nanoparticles.

a) Time			
Fuel	Ratio (Gly/NO_3)	Power (W)	Time (min)
NH_2CH_2COOH	6/3	360	5
NH_2CH_2COOH	6/3	360	10
NH_2CH_2COOH	6/3	360	20
NH_2CH_2COOH	6/3	360	30
b) Power			
Fuel	Ratio (Gly/NO_3)	Power (W)	Time (min)
NH_2CH_2COOH	6/3	180	20
NH_2CH_2COOH	6/3	360	20
NH_2CH_2COOH	6/3	540	20
NH_2CH_2COOH	6/3	720	20
NH_2CH_2COOH	6/3	900	20
c) Type of fuel			
Fuel	Ratio (Gly/NO_3)	Power (W)	Time (min)
NH_2CH_2COOH	6/3	360	20
$CO(NH_2)_2$	6/3	360	20
C_2H_5NO	6/3	360	20
NH_2CH_2COOH	6/3	900	20
$CO(NH_2)_2$	6/3	900	20
C_2H_5NO	6/3	900	20
d) Ratio (Gly/NO_3)			
Fuel	Ratio (Gly/NO_3)	Power (W)	Time (min)
NH_2CH_2COOH	1/1	360	20
NH_2CH_2COOH	6/6	360	20
NH_2CH_2COOH	12/12	360	20
NH_2CH_2COOH	6/3	360	20
NH_2CH_2COOH	3/6	360	20

3) $Bi_2O_3 + Fe_2O_3 \rightarrow 2BiFeO_3$

2.2.1. Preparation of Cu(BDC) using the sonication method

Initially, a total of 2 mmol (0.483 g) of $Cu(NO_3)_2.5H_2O$ and 2 mmol (0.332 g) of terephthalic acid were separately dissolved in 30 mL of N,N-dimethylformamide (DMF). Subsequently, the solution containing the metal salt was added to the ligand solution, and the resulting mixture was subjected to stirring for 15 min. The resulting solution was then subjected to ultrasonic irradiation for 1 h at a power level of 300 W, inducing a phenomenon known as cavitation. During ultrasonic cavitation, transient micro hot spots are generated, exhibiting temperatures of approximately 5000 °C at pressures of 1000 atm, with heating and cooling rates exceeding 1010 K/s. The remarkable consequence of coupling this high temperature with the localized temperature is the disruption of nanoparticle clusters, leading to the production of smaller particles ranging from nanoscale to microscale. The final residue obtained from the reaction was later washed with DMF and subsequently dried in an oven at 220 °C for 20 min. The synthetic pathway is depicted in Scheme ESI 2 for visual reference.

2.3. Preparation of Cu(BDC) using the microwave method

In the initial step, 2 mmol (0.483 g) of Cu $(NO_3)_25H_2O$, 2 mmol (0.332 g) of terephthalic acid were individually dissolved in 30 mL of N,N-dimethylformamide (DMF). Subsequently, the solution of the metal salt was combined with the ligand solution, and the resulting mixture underwent stirring for 15 min. The resulting solution was then transferred to a microwave oven and subjected to microwave irradiation at a power of 300 W for 1 h. The final precipitate obtained was thoroughly washed with DMF multiple times and subsequently dried in an oven at 220 °C for 20 min. The synthetic pathway is depicted in Scheme ESI 3 for illustrative purposes.

2.4. Preparation of $BiFeO_3$/Cu(BDC) nanocomposite using ex-situ microwave method (1)

To prepare the Cu(BDC) solution, 2 mmol (0.483 g) of Cu $(NO_3)_25H_2O$, 2 mmol (0.332 g) of terephthalic acid were separately dissolved in 20 mL DMF. The solutions were then combined under stirring at a temperature of 110 °C. After 30 min, the resulting precipitate was filtered. The obtained solution served as the starting material for synthesizing the composite. For the composite synthesis, 0.1 g of as-prepared $BiFeO_3$ nanoparticles were dispersed in 20 mL of DMF using sonication for 1 h. Subsequently, the $BiFeO_3$ nanoparticle suspension was added to the Cu(BDC) MOF solution and stirred for 1 h. The mixture was then subjected to microwave irradiation at 300 W for 1 h. The final product was thoroughly washed with DMF multiple times and dried in an oven at 220 °C for 20 h. The same synthesis route was repeated using 0.05 g of as-prepared $BiFeO_3$ nanoparticles. Since the resulting products were indistinguishable in both pathways, the composite containing 0.05 g of $BiFeO_3$ nanoparticles was selected for further experimental investigations. The synthesis route is demonstrated in Scheme ESI 4.

2.5. Preparation of $BiFeO_3$/Cu(BDC) nanocomposite using ex-situ sonication method (2)

The preparation of $BiFeO_3$ and Cu(BDC) solutions followed the previously described ex-situ microwave method. Both solutions were individually prepared using the same procedure. Subsequently, the two solutions were combined and subjected to ultrasonic waves at a power of 300 W for 1 h. The resulting precipitate was thoroughly washed with DMF multiple times and then dried in an oven at 220 °C for 20 h. Procedure above, was also repeated using 0.05 g of $BiFeO_3$ nanoparticles. As the final products obtained from both pathways were identical, the composite containing 0.05 g of $BiFeO_3$ nanoparticles content was selected for further experimental investigations. Scheme ESI 5 exhibits the synthetic route, portraying a concise and replicable sequence of chemical reactions and transformations for the desired compound.

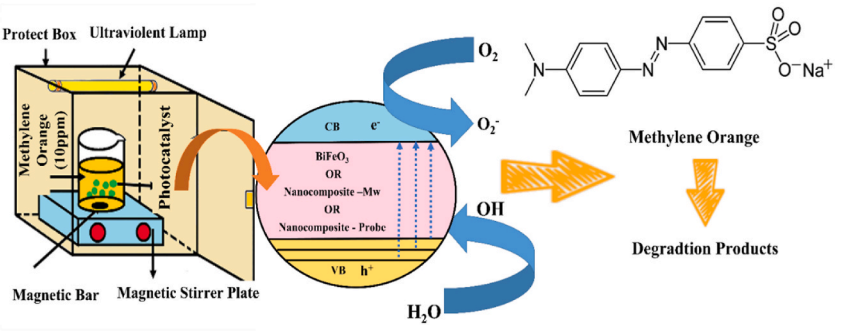

Scheme 1. The graphical illustration for photocatalysis mechanism methylene orange.

2.6. Photocatalysis performance

To evaluate the photocatalytic efficiency of the synthesized materials in the degradation of water contaminants, a catalyst mass of 0.05 g was dispersed in 50 mL of wastewater containing the pollutant as mentioned above, at a concentration of 10 ppm. This mixture was allowed to equilibrate in the absence of light for 1 h. Subsequently, the solution was subjected to visible light irradiation emitted by a mercury lamp. Throughout the process, periodic sampling was performed at predetermined time intervals. The progression of adsorption was monitored using UV–Vis absorption spectroscopy, capturing the changes in absorbance over time (Scheme 1).

3. Results and discussion

3.1. Characterization of $BiFeO_3$

$BiFeO_3$ exhibits a rhombohedral distorted perovskite structure, characterized by its space group *R*3*c*. The lattice parameters for the rhombohedral unit cell are determined as $a_r = 5.63$ Å, $\alpha_r = 59.350$ Å and $a_{hex} = 5.58$ Å, $C_{hex} = 13.87$ Å, respectively. This substance illustrates max polarization in the range of 90–100 μ/cm^2 along the [111] planes at room temperature. The magnetic properties of $BiFeO_3$ are influenced by oxygen defects, resulting in the formation of Fe_2O_3 impurities. The oxygen molecules adopt an octahedral geometry close to the transition metal cations, exhibiting rotational motion either in a clockwise or counterclockwise direction around this axis [47].

IR: Fig. 1 displays the Fourier Transform Infrared (FT-IR) spectrum of the synthesized $BiFeO_3$. The intense peaks at 440 and 560 cm^{-1} are related to forming FeO_6 groups in the perovskite compounds. Through heat treatment, the hydroxyl groups and residual water molecules present in the samples are eliminated, which can be identified in the spectral region of 3400–3500 cm^{-1} and 1610 cm^{-1}. Elevated solution temperature promotes the deprotonation and hydroxylation of metal ions. The FT-IR spectrum depicted in Fig. 1 exhibits significant intensity peaks at 1699 and 1400 cm^{-1}, attributed to the νs(C–O) and νs(C–O) vibrations of carboxylate groups. The carboxylate ion, COO^-, acts as bridging linkers coordinated to Cu nodes, adopting a syn-syn configuration. Additionally, vibration bands observed at 1512 and 746 cm^{-1} correspond to phenyl groups. The FT-IR spectra confirm the presence of characteristic peaks from both components of the as-prepared composites, affirming the successful formation of the composites through ex-situ microwave and ex-situ sonication methods.

XRD: Fig. 2 illustrates the X-ray Diffraction (XRD) pattern of $BiFeO_3$. The crystallographic data of the resultant compound had high adaptation to (ASTM card No.01-086-1518). The diffraction peaks at 2Θ value of 22.41°, 31.75°, 32.06°, 38.95°, 39.48°, 45.45°, 50.37°, 51.31°, 51.73°, 56.36°, 56.96°, 66.34°, and 67.06° related to planes (012), (104), (110), (006), (202), (024), (211), (116), (122), (018), (214), (208) and (220), respectively. It should be noted that the presence of a diffraction peak at $2\theta = 27.82°$ indicates the existence of Bi_2O_3 impurities in the synthesized product. The XRD pattern of Cu(BDC) was also included to examine its phase purity, revealing no impurities within the framework phase. The peaks at $2\theta = 9.1°$ and 8.3° correspond to the crystallographic planes (001) and (020), respectively. To confirm the formation of composites 1 and 2, XRD patterns of both composites were recorded. The newly obtained patterns exhibit characteristic peaks of the Metal-Organic Framework (MOF) and bismuth ferrite nanoparticles, confirming the successful preparation of the proposed composites.

SEM: Fig. 3 showcases the scanning electron microscope (SEM) images, revealing the porous structure of the as-prepared bismuth ferrite. This distinctive structure emerges from the agglomeration of bismuth ferrite nanoparticles during gas emissions. The particle size distribution is presented in Fig. 3(d), indicating the presence of nanoparticles with sizes ranging from 40 to 45 nm. SEM images of the Cu(BDC) framework synthesized using microwave synthesis and sonication methods are displayed in Fig. 3e and f, respectively. Both images demonstrate the presence of uniformly shaped cubic particles. Furthermore, SEM images of composites 1 and 2 were captured and depicted in Fig. 3g and h. It can be observed that the incorporation of bismuth ferrite nanoparticles alters the cubic form of the Cu(BDC) structure. Notably, composite 2, synthesized through the sonication method, exhibits a slightly smaller particle size compared to composite 1.

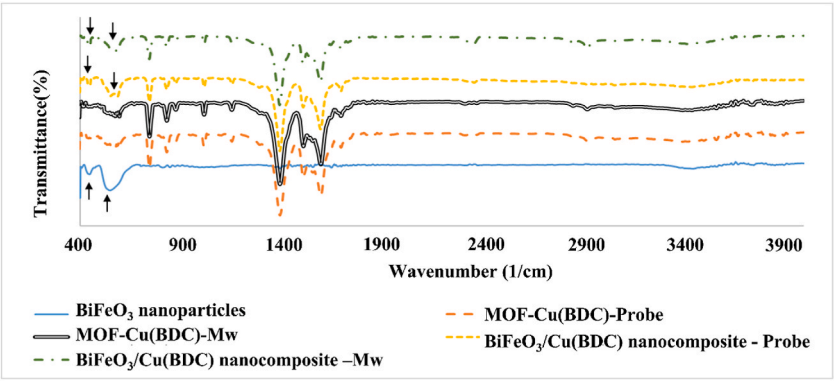

Fig. 1. FTIR spectra of as-prepared materials.

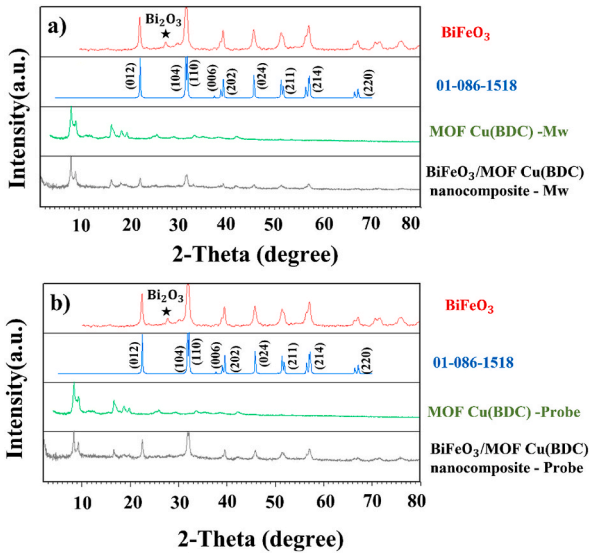

Fig. 2. The powder XRD patterns of as-prepared materials.

DRS: UV-DRS spectroscopy was employed to investigate the optical properties and band gap characteristics of the synthesized $BiFeO_3$ NPs, Cu(BDC), and the resulting composites. The recorded spectra covering a wavelength range of 200–800 nm are depicted in Fig. 4. The band gap, representing the energy difference between the valence band and conduction band in semiconductors or insulators, was determined from the DRS curve of $BiFeO_3$ NPs, yielding a calculated value of 1.75 eV. This result confirms the semiconducting nature of $BiFeO_3$ NPs. It is noteworthy that the measured band gap is smaller compared to $BiFeO_3$ films (2.5 eV), potentially attributed to the thin film sample's reduced thickness, which enhances the absorption of visible light and holds promise for efficient photocatalysis. Furthermore, the UV-DRS spectrum of the Cu(BDC) MOF was obtained, allowing the determination of its color based on the emission's λ_{max}. The recorded spectrum reveals a λ_{max} of approximately 490 nm, indicating that Cu(BDC) exhibits a blue color. The UV-DRS curves of the prepared composites show noticeable changes compared to the individual components. As the MOF acts as the primary matrix of the composites, the DRS spectra of the composites closely resemble that of the MOF. However, slight variations in the spectra of the composites can be attributed to differences in particle size and the synthesis methods employed for their preparation.

VSM: The magnetic properties of the synthesized $BiFeO_3$ NPs and the resulting composites were characterized using a vibrating sample magnetometer (VSM), and the corresponding magnetization data as a function of the applied magnetic field are plotted in Fig. 5. The rhombohedral distorted perovskite structure of $BiFeO_3$ gives rise to weak ferromagnetic ordering due to spin canting. This weak ferromagnetic behavior can be attributed to the noncollinear (canted) spin arrangements within the two sublattices. The small magnetic moment direction results in a spiral spin arrangement with an average crystallite size of 62 nm, leading to a helimagnetic order and negligible bulk magnetization. Furthermore, for crystallite sizes smaller than 62 nm, $BiFeO_3$ displays weak ferromagnetic behavior from incomplete spin rotation along the antiferromagnetic axis. At room temperature, $BiFeO_3$ exhibits antiferromagnetic properties. As the particle size decreases, paramagnetic properties become more prominent in these nanoparticles. The hysteresis loop of $BiFeO_3$, as shown in Fig. 5, appears narrow and sharp, indicating its characteristics as a soft magnetic material. In Fig. 5c and d, the hysteresis loops of composites 1 and 2 are provided, revealing slight magnetic properties. This confirms the presence of $BiFeO_3$ NPs and Cu(BDC), as well as the magnetization of the MOF component in the composites.

ICP: The quantification of bismuth (Bi) content in the $BiFeO_3$ nanoparticles was carried out using ICP analysis with standard samples of $Bi(NO_3)_3{\cdot}5H_2O$. The resulting data, indicating the concentration of Bi, are compiled in Table 2.

3.2. Photocatalysis investigations

To evaluate the photocatalytic performance of $BiFeO_3$ nanoparticles and the resulting composites, 0.05 g of $BiFeO_3$, nanocomposite 1, and nanocomposite 2 were individually exposed to a 50 mL solution of methyl orange with a concentration of 10 ppm. Fig. 6 presents the UV–Vis spectra depicting the degradation of methyl orange by the substances under various light radiation conditions. It can be observed that both nanocomposite 1 and 2 exhibit enhanced photocatalytic properties compared to $BiFeO_3$ alone. Furthermore, Fig. 6 also displays the kinetic plots of the degradation process for nanocomposite 1 and nanocomposite 2. These plots provide valuable insights into the reaction kinetics and demonstrate the improved photocatalytic efficiency of the composites. Kinetic plots of their reaction rate per time in a certain concentration are calculated according to equation (1):

$$C_t = [A_1 \times C_0]/A_0 \quad (1)$$

Where C_t is the pollutant concentration at the moment, A_1 is the amount of adsorption at the moment, and C_0 points to the initial concentration of the pollutant. The percentages of pollutant degradation at different times have been collected in Table 3. The initial

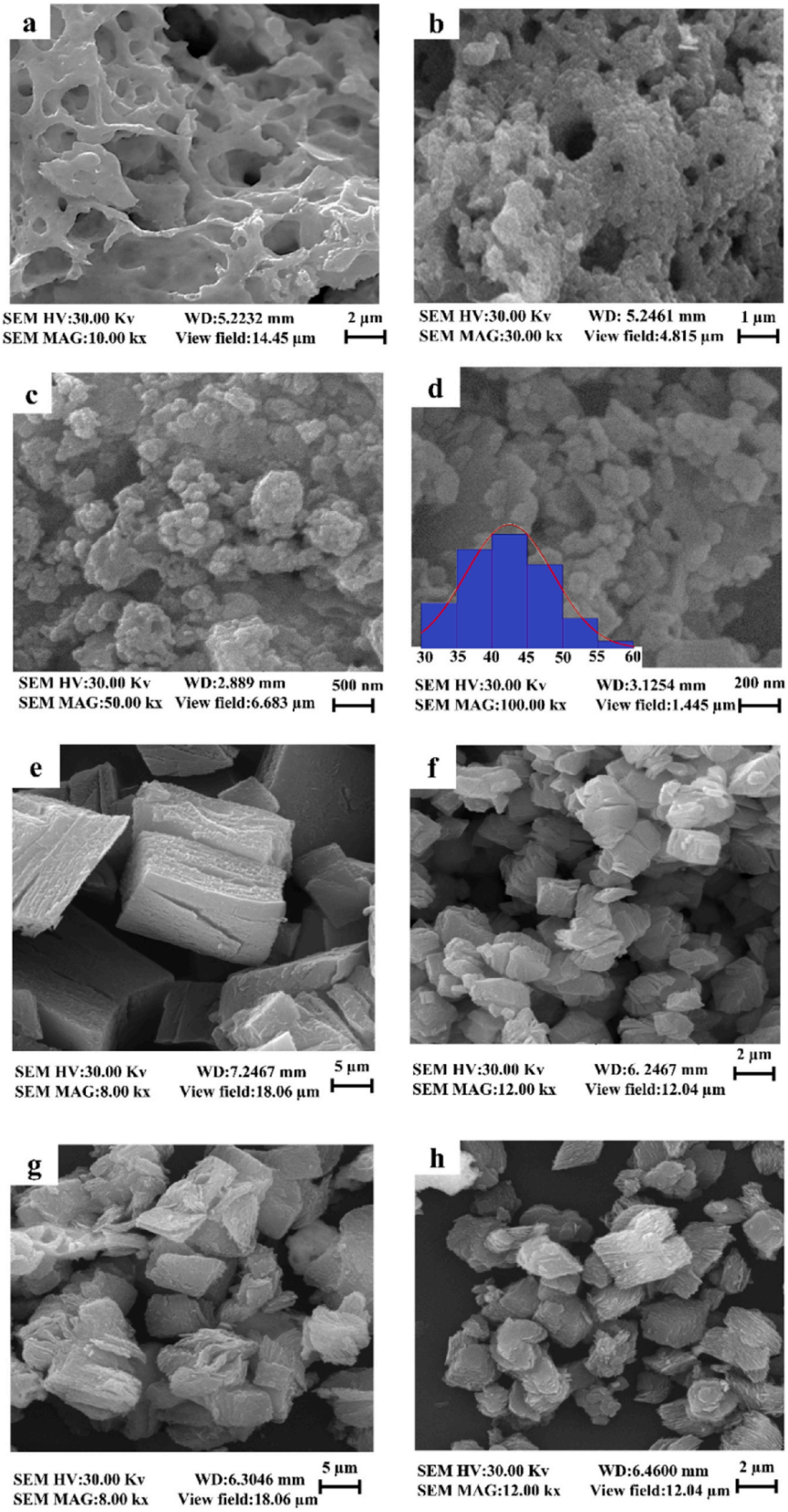

(caption on next page)

Fig. 3. SEM images of as-prepared materials. a-d) $BiFeO_3$ nanoparticles, e) Cu(BDC) framework synthesized by microwave method, f) Cu(BDC) framework synthesized by sonication method, g) nanocomposite synthesized ex-situ microwave method, h) nanocomposite synthesized ex-situ sonication method.

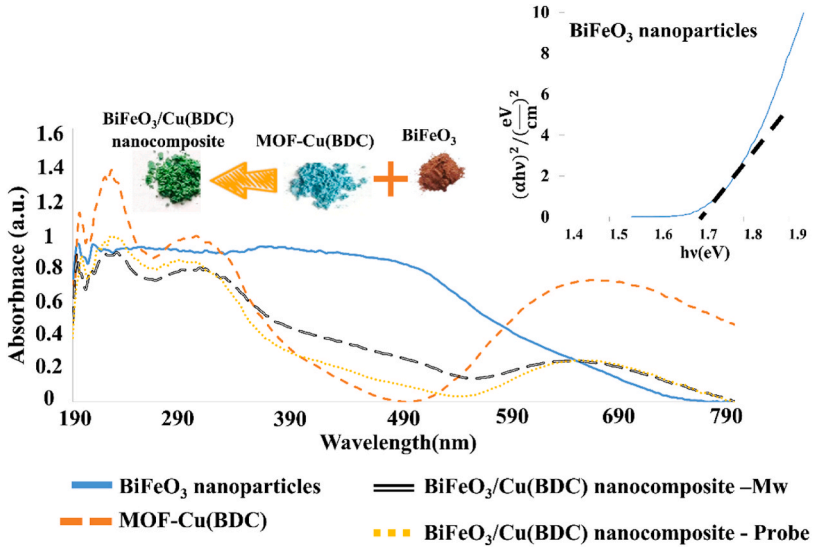

Fig. 4. DRS spectra of as-prepared materials.

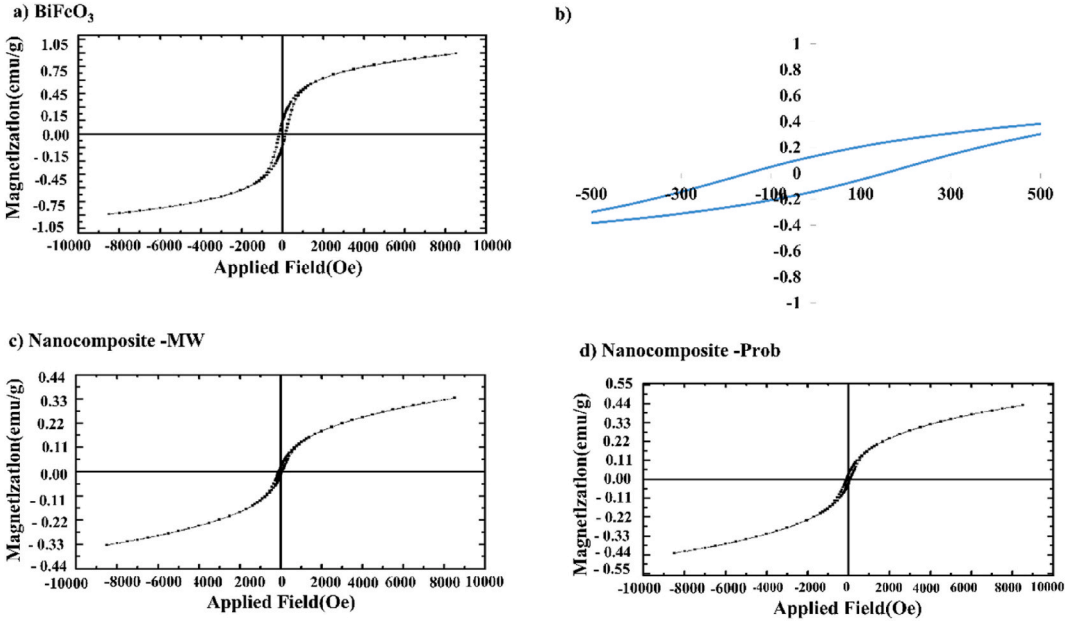

Fig. 5. VSM plots of a and b) hysteresis loop $BiFeO_3$ nanoparticles, c) nanocomposite 2 and d) nanocomposite 1.

concentration for R_f calculation, the concentration after passing 1 h in the dark, was considered.

Fig. 7 displays the kinetic trends of the degradation process within a 60-min timeframe. The plot provides a visual representation of the degradation rates of the studied substances over time, allowing for a comprehensive analysis of their photocatalytic performance.

The proposed mechanism elucidating the degradation process of methyl orange utilizing nanocomposites consisting of bismuth ferrite and the metal-organic framework Cu(BDC) is presented as follows:

1) **Nanocomposite BiFeO$_3$/Cu(BDC)** + **hν**→**BiFeO$_3$/Cu(BDC)**(e^-_{CB} + h^+_{VB}) trapping sites
2) **BiFeO$_3$/Cu(BDC)**(e^-_{CB}) trapping sites + **O$_2$**→**$O_2^{\cdot-}$**.

Table 2
Collects the amount of Bi in $BiFeO_3$ nanoparticles.

Materials	Theoretical Concentration Bi (ppm)	Experimental Concentration Bi (ppm)	Error (%)
$BiFeO_3$	**20**	**19.60**	**2**
Nanocomposite-MW-0.05	**20**	**17.02**	**14**
Nanocomposite -Probe-0.05	**20**	**16.23**	**18**

3) $\mathbf{O_2^{\cdot-} + H_2O \rightarrow OH_2^{\cdot} + OH^{\cdot}}$.

4) $\mathbf{OH_2^{\cdot} + H_2O \rightarrow OH^{\cdot} + H_2O_2}$.

5) $\mathbf{H_2O_2 \rightarrow 2OH^{\cdot}}$.

6) $\mathbf{BiFeO_3/Cu(BDC)(h_{VB}^{+}) + H_2O \rightarrow OH^{\cdot}}$.

7) $\mathbf{BiFeO_3/Cu(BDC)(h_{VB}^{+}) + Methyl\ orange(MO) \rightarrow CO_2 + H_2O}$.

8) $\mathbf{O_2^{\cdot-}\ or\ OH^{\cdot}\ or\ OH^{\cdot} + Methyl\ orange(MO) \rightarrow CO_2 + H_2O}$.

Furthermore, the structural conversion of methyl orange into carbon dioxide and water is facilitated by the generated radicals, as depicted in Fig. 8.

A comparison between the work done in this research with the other bismuth ferrite nanocomposites was given in Table 4. The photocatalytic performance of the nanocomposite catalyst consisting of Graphitic carbon nitride/bismuth ferrite ($g\text{-}C_3N_4/BiFeO_3$) was evaluated for the degradation of methyl orange (MO) under UV and visible light. Destruction under UV light necessitated a 300 W high-pressure Hg lamp, while visible light was achieved using a 500 W xenon lamp with a 420 nm cutoff filter. The nanocomposite achieved an approximate 63 % degradation of MO [71].

Bajpai and colleagues have also contributed to research in this field. This research group synthesized bismuth ferrite nanoparticles grafted on graphene nanosheets ($BiFeO_3$-g-GNS) and examined the photocatalytic performance of $BiFeO_3$-g-GNS for degrading methyl orange. Visible light irradiation was conducted using a 300 W halogen lamp with a wavelength of 420 nm. The $BiFeO_3$-g-GNS photocatalyst achieved a degradation efficiency of approximately 35.9 % for methyl orange dye [72].

In a study undertaken in 2020, the catalyst used was a nanocomposite material consisting of bismuth ferrite nanoparticles grafted on graphene oxide (BFO-GO9%). Photocatalytic degradation of methyl orange (MO) dye and methylene blue (MB) dye was performed under ambient sunlight. The percentage of destruction of methyl orange using the BFO-GO9% photocatalyst was approximately 57 % [73].

The experimental findings of this research project clearly demonstrated that the utilization of bismuth ferrite nanocomposites within an organic metal framework outperforms the efficacy of reported graphitic structures in the photocatalytic degradation of methyl orange. This enhanced performance extends beyond the graphitic structures bismuth ferrite nanocomposite investigated in this study and encompasses other nanocomposites incorporating bismuth ferrite with various metal oxides. For instance, Skiker conducted research on the photocatalytic degradation of methyl orange (MO) dye using the $Bi1_2TiO_{20}/BiFeO_3$ nanocomposite, achieving a degradation rate of approximately 68 % [74]. Similarly, in another study by Samran, the $0.6BiFeO_3$-$0.4Bi_2WO_6$ nanocomposite exhibited a lower rate of destruction, with only 54 % degradation of MO dye within 2 h under sunlight [75]. These findings further emphasize the enhanced efficacy of bismuth ferrite nanocomposites within an organic metal framework for efficient degradation of organic pollutants. Recently, Moradi and his colleagues have investigated the photocatalytic degradation of methyl orange on various bismuth ferrite nanocomposites. In their studies, it has been observed that $BiFeO_3$ combined with polyethylene glycol-PEG-6000 ($BiFeO_3$-PEG) exhibits approximately 67 % degradation, while the nanocomposite demonstrates around 72 % degradation over a longer period of 4 h [76].

3.3. Adsorption investigations

As-synthesized $BiFeO_3$ nanoparticles were dispersed in a freshly prepared aqueous solution containing 10 parts per million (ppm) of Congo red. Subsequently, 0.05 g of $BiFeO_3$ were added to 50 mL of the Congo red solution under gentle magnetic stirring in a dark environment. For 3 h, a significant color change was observed, wherein the Congo red solution exhibited a dramatic transition from a red hue to a colorless state. This transformation was meticulously monitored using UV–Vis absorption spectroscopy, and the collected data is presented in Fig. 9 a. The effectiveness of this method was evaluated on various other wastewater pollutants, including Brilliant Blue, Malachite Green, and Methylene Blue. However, among the tested pollutants, Congo red demonstrated the most favorable response, thereby justifying its selection for further experimental investigations. To establish comparability, the initial concentration of Congo red was adjusted to 300 ppm by increasing its concentration and allowing the process to proceed for 1 h without light. Importantly, the addition of $BiFeO_3$ nanoparticles, coupled with gentle magnetic stirring, resulted in the efficient adsorption of Congo red, as depicted in Fig. 9 b. Considering that Beer-Lambert's law exhibits linear behavior within a certain concentration range, dilution ratios were employed to accommodate higher concentrations. To gain insight into the adsorption process facilitated by the prepared adsorbents, it is essential to elucidate the underlying adsorption mechanisms. Notably, Langmuir and Freundlich adsorption isotherms are commonly employed to provide valuable information regarding the adsorption mechanism, the affinity of the adsorbent, and the surface properties. After 1 h of dark incubation, the equilibrium solution concentration was determined. Fig. 9 c and 9.d illustrate the Langmuir and Freundlich isotherms, respectively. Based on the coefficient of determination (R^2) values, the Langmuir isotherm was

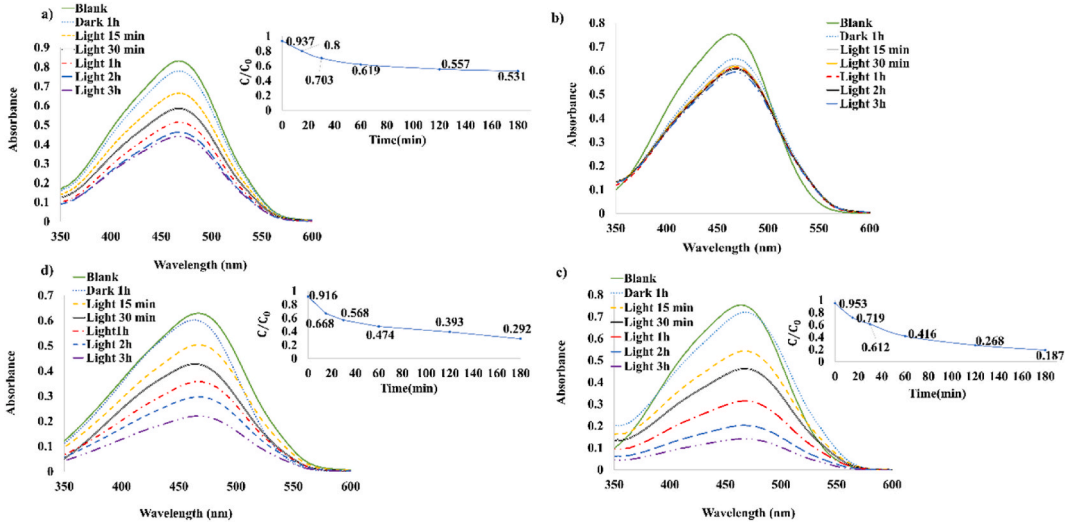

Fig. 6. UV–Vis spectra of methyl orang degradation using a) $BiFeO_3$, b) MOF, Cu(BDC), c) nanocomposit 1 and d) nanocomposite 2 during 3 h of light radiation.

Table 3
The degradation percentage in the various times with 0.05 g of the catalyst.

Catalyst	Degradation (%) 15min	Degradation (%) 30min	Degradation (%) 60min	Degradation (%) 120min	Degradation (%) 180min
$BiFeO_3$	**19.97**	**29.60**	**38.02**	**44.22**	**46.81**
Nanocomposite-MW - 0.05	**28.02**	**38.77**	**58.43**	**73.17**	**81.27**
Nanocomposite-Probe - 0.05	**33.20**	**43.21**	**52.58**	**60.69**	**70.78**

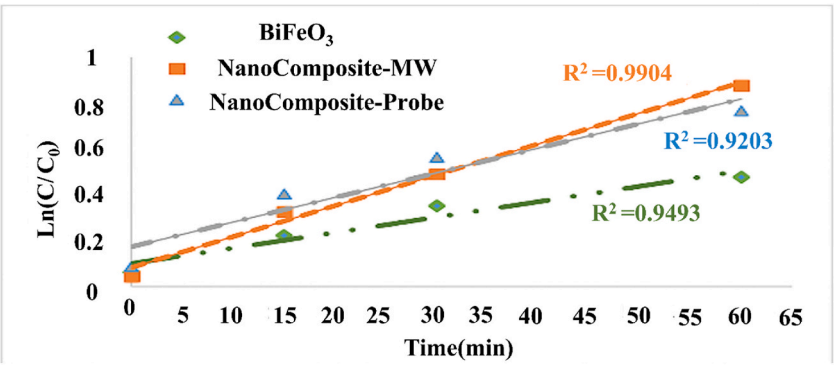

Fig. 7. Kinetic trend of methyl orang degradation.

more suitable than the Freundlich isotherm for describing the adsorption process of Congo red onto the as-synthesized $BiFeO_3$ adsorbents.

In the subsequent phase, the adsorption process was replicated using Cu(BDC) to assess its adsorption efficiency. To facilitate a more accurate comparison, the sampling was conducted for 1 h. The obtained results are presented in Fig. 10. Unlike the $BiFeO_3$ compound, the Freundlich isotherm was appropriate than the Langmuir isotherm in describing the adsorption process of Congo red on as-synthesized Cu(BDC) adsorbents. Fig. 11a and b presents the adsorption performance of the as-prepared composites towards Congo red under the aforementioned conditions.

The parameters for the Freundlich and Langmuir adsorption models, on the adsorption of Congo red, are provided in Table 5.

To investigate the placement of Congo red on a magnetic adsorbent, a comprehensive mass analysis was conducted on the structure of Congo red, as well as its bismuth ferrite nanocomposite synthesized through both microwave and ultrasonic methods. The obtained results, depicted in Fig. 12, demonstrate observable interactions between Congo red and the synthesized nanoabsorbents. The spectra of pure Congo red and after use have come out to be identical and show the presence of dye on the surface of catalyst, thus confirming the process of adsorption of dye. The molecular mass of Congo red, determined to be 652. A peak at 651 m/z was observed due to

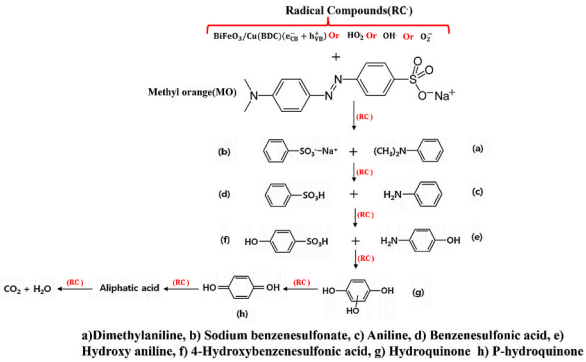

Fig. 8. Degradation of methyl orange a)dimethylaniline, b) sodium benzenesulfonate, c) aniline, d) benzenesulfonic acid, e) hydroxy aniline, f) 4-hydroxybenzenesulfonic acid, g) hydroquinone, h) p-hydroquinone.

Table 4
Comparison with the other bismuth ferrite nanocomposites.

Photocatalyst	Degradation (%)	Method	Time (min)	Pollutant	Refs.
g-C_3 N_4 -$BiFeO_3$	63	visible light)500 W xenon lamp(	120	Methyl Orange	[71]
$BiFeO_3$-g-GNS	36	visible light (l Z 420 nm, 300 W halogen lamps)	60	Methyl Orange	[72]
$BiFeO_3$-GO9%	57	visible light (under direct sunlight irradiation)	120	Methyl Orange	[73]
0.55 $Bi1_2TiO_{20}$ 0.45 $BiFeO_3$	68	UV irradiation source (mercury lamp 125 W)	120	Methyl Orange	[74]
0.6$BiFeO_3$-0.4Bi_2WO_6	54	visible light (50 W halogen lamp)	120	Methyl Orange	[75]
$BiFeO_3$-PVA	72	UV irradiation (10 W LED lamp)	240	Methyl Orange	[76]
$BiFeO_3$-PEG	67				
Nanocomposite-MW - 0.05	74	visible light (50 W halogen lamp)	120	Methyl Orange	**This work**
Nanocomposite-Probe - 0.05	61				

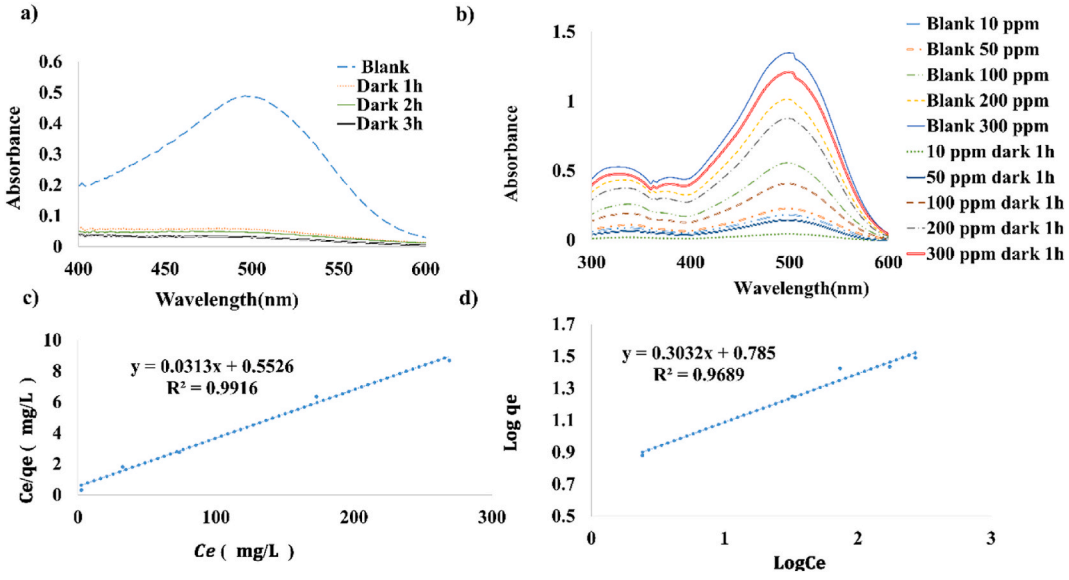

Fig. 9. Congo red adsorption using $BiFeO_3$ a) various time for 10 ppm initial concentration b) various initial concentration after 1 h in dark, c) Langmuir isotherm and d) Freundlich isotherm.

remove a proton (H^+) from Congo red molecule. The presence of a peak at 571 m/z, indicating the detachment of an SO_3 group from its structure. Another peak at 491 m/z suggested the detachment of two SO_3 groups. Notably, characteristic peaks in the range of 621 to 593 m/z were attributed to the loss of one or both N_2 and NH_2 moieties from the structure. Moreover, the removal of one SO_3 group in conjunction with one N_2 or NH_2 led to a discernible peak at 543 m/z, and the detachment of one SO_3 group and one SO_2 group resulted in a peak at 507 m/z. Additionally, the removal of two SO_3 groups and one N_2 produced a characteristic peak at 463 m/z, and the removal of two SO_3 groups combined with both N_2 groups generated a peak at 432 m/z. Apart from these observations, Congo red

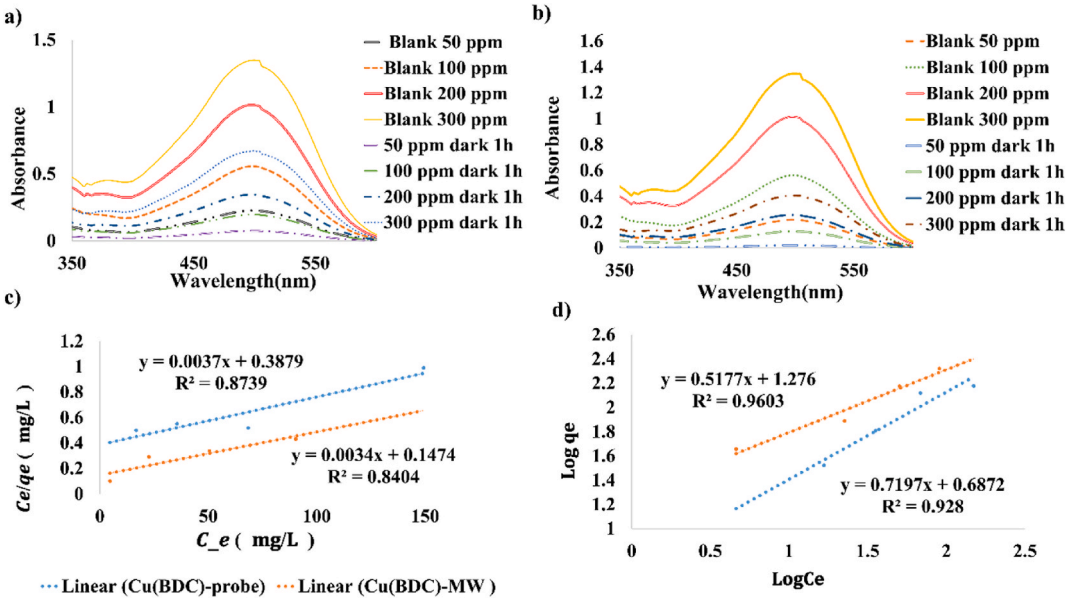

Fig. 10. Congo red adsorption using a) Cu(BDC)-MW and b) Cu(BDC)-probe, c) Langmuir isotherms and d) Freundlich isotherms.

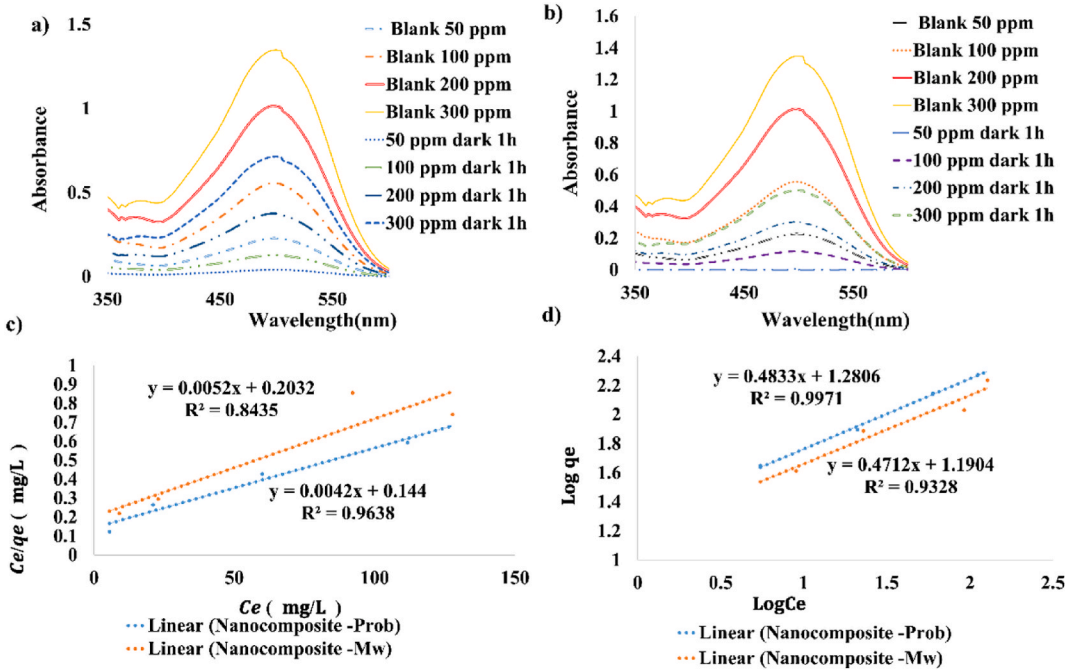

Fig. 11. Adsorption performance of a) nanocomposite 1 and b) nanocomposite 2, c) Langmuir isotherm and d) Freundlich isotherm.

exhibited the other fragmentation, leading to the formation of radical structures with molecular masses of 416,234, 233, and 235 m/z [77]. The other peaks that can be seen in the spectrum refer to the complexity and broadening of the obtained spectrum were attributed to various probable reactions forming these radical structures and their resulting products, as well as reactions involving compound detachment and rearrangements. It was also noted that impurity peaks might be present in the spectrum [78]. The catalytic effect of the copper atom in the framework of the organic metal Cu(BDC) can also be effective in the surface absorption process and cause peaks in the region of 271, 169, 173 and 150 m/z. Possible fragmentations of CR were shown in Table 6.

Assessing the reusability of adsorbents is a crucial factor in determining their commercial viability. Leveraging the magnetic properties of the prepared adsorbent, an external magnetic field was applied to facilitate the collection of adsorbents post-adsorption process. However, due to $BiFeO_3$ exhibiting a weak adsorption capacity, the evaluation of its reusability behavior was not conducted.

Table 5
The parameters of mechanism Freundlich and Langmuir for Adsorption Congo red.

Adsorbent	Freundlich			Langmuir			
	n	K_F	R^2	q_m(mg g^{-1})	a_L	K_L (L m g^{-1})	R^2
$BiFeO_3$	**3.29**	**6.095**	**0.9689**	**31.95**	**0.056**	**1.808**	**0.9916**
MOF-Cu(BDC)-Probe	**1.38**	**4.866**	**0.9280**	**270.27**	**0.001**	**2.577**	**0.8739**
MOF-Cu(BDC)-MW	**1.93**	**18.879**	**0.9603**	**294.11**	**0.021**	**6.784**	**0.8404**
Nanocomposite-Probe-0.05	**2.06**	**19.080**	**0.9971**	**238.01**	**0.029**	**6.944**	**0.9639**
Nanocomposite -MW-0.05	**2.12**	**15.503**	**0.9328**	**192.30**	**0.025**	**4.921**	**0.8435**

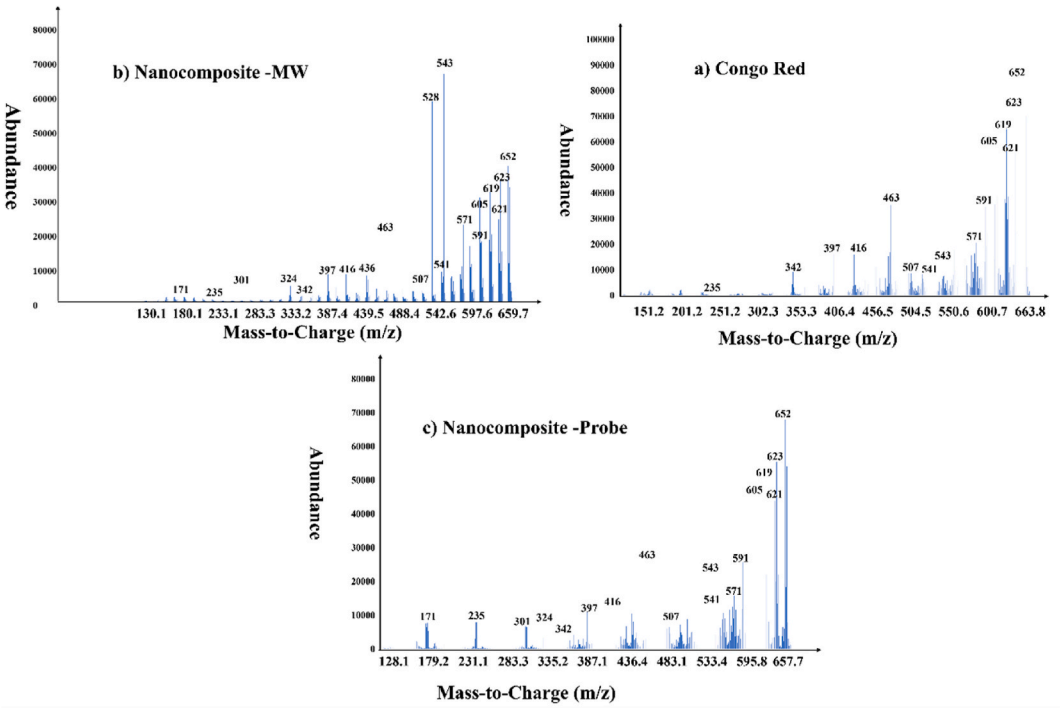

Fig. 12. Mass spectrum of a) Congo red b) nanocomposite MW c) nanocomposite prob.

After the adsorption process, the adsorbents underwent a thorough washing procedure involving water, ethanol, acetone, and DMF, followed by drying at 220 °C. The adsorbents were subjected to consecutive exposure to the contaminant without further purification. This cyclic process was repeated three times for all three adsorbents, and the results are graphically represented in Fig. 13a–d. Apart from physical adsorption, the adsorption of Congo red may involve chemical interactions with the metal-organic framework (MOF). The presence of π electrons in the BDC linker of the MOF facilitates adsorption through π-π interactions, contributing to the overall adsorption process. As depicted in Fig. 13, the reusability of the adsorbents exhibits a decreasing trend, which can be attributed to the inherent instability of the organic metal framework Cu(BDC). This instability arises from the susceptibility of Cu(BDC) to hydrolysis reactions, particularly in the presence of moisture or aqueous environments. The copper-carboxylate bonds within the MOF structure are vulnerable to hydrolytic cleavage when exposed to water molecules. This degradation process occurs due to a nucleophilic attack by water molecules on the copper ions, leading to the dissociation of metal-carboxylate coordination bonds. Consequently, the MOF structure experiences a loss of structural integrity, thereby compromising the stability and functionality of Cu(BDC) [79,80].

3.4. Electrochemical measurement

The electrochemical behavior was assessed through cyclic voltammetry (CV) analysis employing a 3-electrode setup consisting of platinum (Pt) and silver/silver chloride (Ag/AgCl) electrodes as the counter and reference electrodes, respectively. The tests were conducted in 0.1 M electrolyte solutions comprising various species such as potassium hydroxide (KOH), sulfuric acid (H_2SO_4), and lithium perchlorate ($LiClO_4$), with scan rates of 0.05, 0.1, and 0.2 mV s^{-1}. The potential window for the measurements ranged from −0.4 to 0.8 V. Two different synthesis methods, sonication and microwave, were employed to obtain the bismuth ferrite nanoparticles and the as-synthesized nanocomposites. The selected electrolytes were potassium hydroxide, sodium sulfate, and lithium perchlorate. Fig. 14 illustrates that lithium perchlorate exhibited the highest current density compared to the other electrolytes, owing to its strong

Table 6
Fragmentation Congo red.

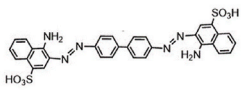	-	652
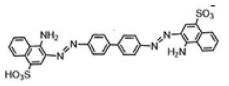	H	651
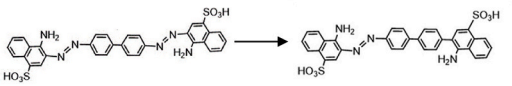	N_2	623
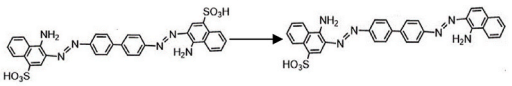	SO_3	571
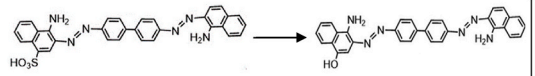	SO_3 , SO_2	507
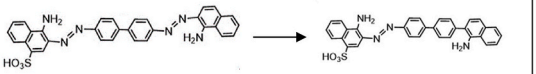	SO_3, N_2	543
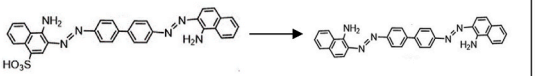	SO_3, SO_3	491
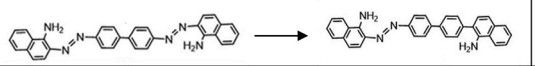	SO_3, SO_3, N_2	463
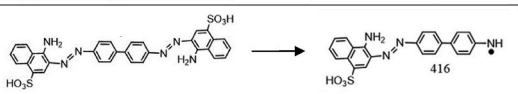	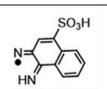	416
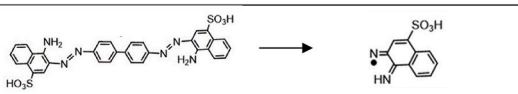	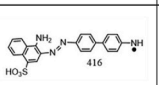	234
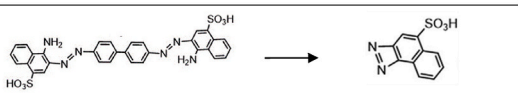	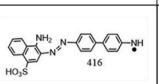	233
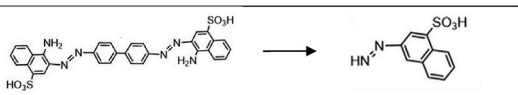	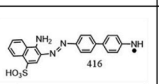	235
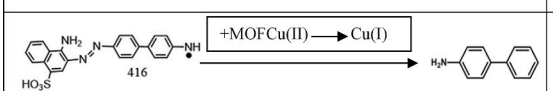		169
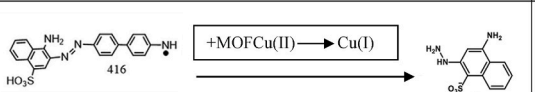	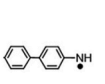	271
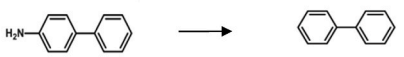	NH_2	153
	SO_3, NH_2H_2	173

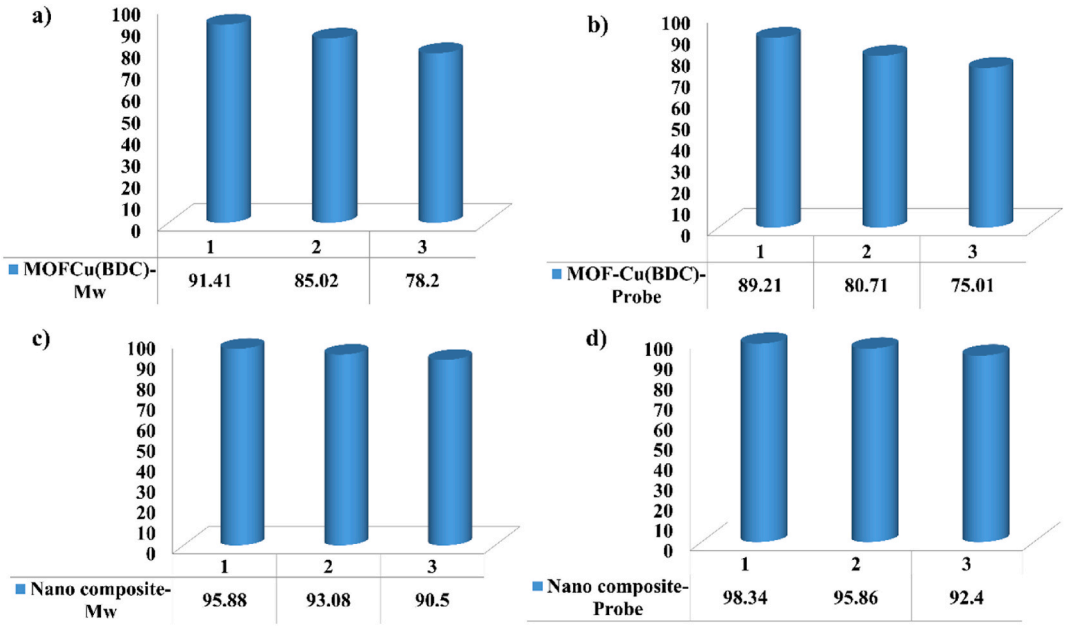

Fig. 13. Reusability tests of a) Cu(BDC)-MW, b) Cu(BDC)-probe, c) nanocomposite 1 and d) nanocomposite 2.

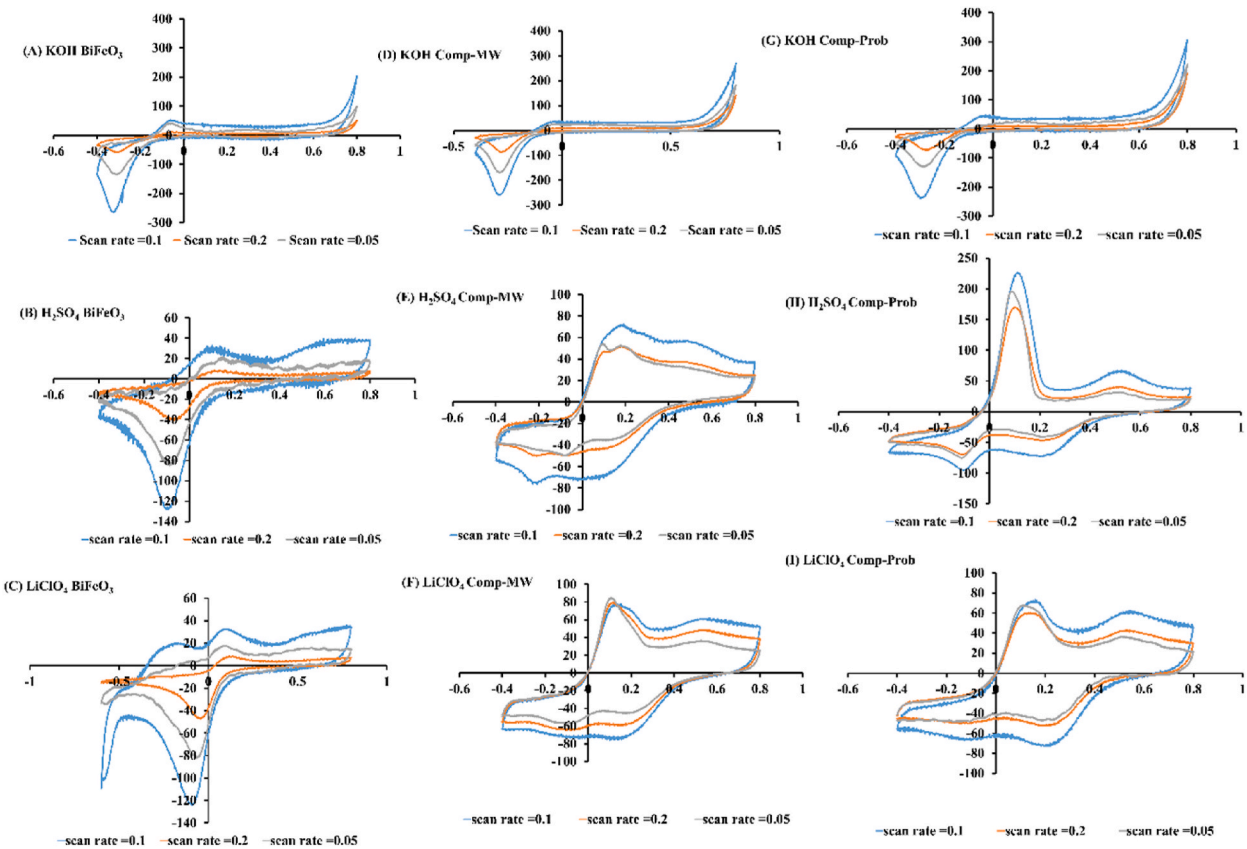

Fig. 14. CV curves of bismuth ferrite nanoparticles, nanocomposite synthesized by microwave method and nanocomposite synthesized by sonication method in the different electrolytes: (a,d,g) KOH, (b,e,h) H_2SO_4, (c,f,i) $LiClO_4$.

oxidizing properties that resulted in an enhanced potential gradient near the electrode surface. At low scan rates (Fig. 14(b) and (c)), the effect of diffusion coefficient differences was found to be statistically insignificant. The optimal scan rate determined in this study was 0.1 mV s^{-1}. A decrease in current density was observed at higher or lower scan rates due to forming a thinner depletion layer and a thicker diffusion layer near the electrode, respectively. However, as depicted in Fig. 14(e) and (f), this effect was also negligible when using the nanocomposite, as the resulting curves closely overlapped. The nanocomposite synthesized via the microwave method exhibited a higher current density, likely attributed to its particle size, facilitating ion transfer. The anodic peaks observed at −0.2 V and 0.1 V, and the cathodic peak at −0.1 V, can be attributed to the oxidation and reduction processes of Bi°(metal) ⇌ Bi^{3+} and Bi^{3+} ⇌ Bi°(metal), respectively. Furthermore, using the nanocomposite induced a positive shift in the potential.

4. Conclusions

In this study, we introduced two novel nanocomposites comprised of $BiFeO_3$ and Cu(BDC) to emphasize the synergistic effect of their combination on photocatalytic activity and adsorption performance. We assessed the effectiveness of these composites in the removal of dye pollutants from wastewater. Notably, the nanocomposites possess magnetic properties, allowing for rapid separation from the solution using an external magnetic field, which is advantageous for potential commercial adsorbents. Based on the results obtained, we assert that these nanocomposites exhibit considerable potential as practical materials for the remediation of dye pollutants in aqueous solutions. In the electrochemical investigations, we determined the optimized scan rate to be 0.1 mV s^{-1}, and the nanocomposite synthesized via the microwave method demonstrated superior current density.

Formatting of funding sources

This research did not receive any specific grant from funding agencies in the public, commercial, or not-for-profit sectors.

CRediT authorship contribution statement

Fatemeh Shahrab: Writing – original draft, Investigation, Formal analysis. **Azadeh Tadjarodi:** Writing – review & editing, Supervision, Project administration, Conceptualization.

Declaration of competing interest

The authors declare that they have no known competing financial interests or personal relationships that could have appeared to influence the work reported in this paper.

Acknowledgment

We gratefully acknowledge Iran University of Science and Technology for providing materials and some facilities.

Appendix A. Supplementary data

Supplementary data to this article can be found online at https://doi.org/10.1016/j.heliyon.2023.e20689.

References

[1] S. Garg, Z.Z. Chowdhury, A.N.M. Faisal, N.P. Rumjit, P. Thomas, Impact of Industrial Wastewater on Environment and Human Health, Advanced Industrial Wastewater Treatment and Reclamation of Water: Comparative Study of Water Pollution Index during Pre-industrial, Industrial Period and Prospect of Wastewater Treatment for Water Resource Conservation, Springer International Publishing, 2022, pp. 197–209, https://doi.org/10.1007/978-3-030-83811-9-10.

[2] L. Lara, I. Cabral, J. Cunha, Ecological approaches to textile dyeing: a review, Sustainability 14 (2022) 8353, https://doi.org/10.3390/su14148353.

[3] A. Gičević, L. Hindija, A. Karačić, Toxicity of Azo Dyes in Pharmaceutical Industry, CMBEBIH 2019: Proceedings of the International Conference on Medical and Biological Engineering, 16-18 May 2019, Banja Luka, Bosnia and Herzegovina, Springer International Publishing, 2020, pp. 581–587, https://doi.org/10.1007/978-3-030-17971-7_88.

[4] R. Al-Tohamy, S.S. Ali, F. Li, K.M. Okasha, Y.A.-G. Mahmoud, T. Elsamahy, H. Jiao, Y. Fu, J. Sun, A critical review on the treatment of dye-containing wastewater: ecotoxicological and health concerns of textile dyes and possible remediation approaches for environmental safety, Ecotoxicol. Environ. Saf. 231 (2022), 113160, https://doi.org/10.1016/j.ecoenv.2021.113160.

[5] S. Sutar, P. Patil, J. Jadhav, Recent advances in biochar technology for textile dyes wastewater remediation: a review, Environ. Res. 209 (2022), 112841, https://doi.org/10.1016/j.envres.2022.112841.

[6] R. Bushra, S. Mohamad, Y. Alias, Y. Jin, M. Ahmad, Current approaches and methodologies to explore the perceptive adsorption mechanism of dyes on low-cost agricultural waste: a review, Microporous Mesoporous Mater. 319 (2021), 111040, https://doi.org/10.1016/j.micromeso.2021.111040.

[7] R. Gondi, S. Kavitha, R.Y. Kannah, O.P. Karthikeyan, G. Kumar, V.K. Tyagi, J.R. Banu, Algal-based system for removal of emerging pollutants from wastewater: a review, Bioresour. Technol. 344 (2022), 126245, https://doi.org/10.1016/j.biortech.2021.126245.

[8] H.K. Okoro, S. Pandey, C.O. Ogunkunle, C.J. Ngila, C. Zvinowanda, I. Jimoh, I.A. Lawal, M.M. Orosun, A.G. Adeniyi, Nanomaterial-based biosorbents: adsorbent for efficient removal of selected organic pollutants from industrial wastewater, Emerging Contam. 8 (2022) 46–58, https://doi.org/10.3390/ASEC2022-13812.

[9] T. Shindhal, P. Rakholiya, S. Varjani, A. Pandey, H.H. Ngo, W. Guo, H.Y. Ng, M.J. Taherzadeh, A critical review on advances in the practices and perspectives for the treatment of dye industry wastewater, Bioengineered 12 (2021) 70–87, https://doi.org/10.1080/21655979.2020.1863034.

[10] H.A.P. Dos Santos, A.B. de Castilhos Júnior, W.C. Nadaleti, V.A. Lourenço, Ammonia recovery from air stripping process applied to landfill leachate treatment, Environ. Sci. Pollut. Control Ser. 27 (2020) 45108–45120, https://doi.org/10.1007/s11356-020-10397-9.

[11] Z. Iqbal, M.S. Tanweer, M. Alam, Recent advances in adsorptive removal of wastewater pollutants by chemically modified metal oxides: a review, J. Water Proc. Eng. 46 (2022), 102641, https://doi.org/10.1016/j.jwpe.2022.102641.

[12] Z. Yang, Y. Zhou, Z. Feng, X. Rui, T. Zhang, Z. Zhang, A review on reverse osmosis and nanofiltration membranes for water purification, Polymers 11 (2019) 1252, https://doi.org/10.3390/polym11081252.

[13] J. El-Gaayda, F.E. Titchou, R. Oukhrib, P.-S. Yap, T. Liu, M. Hamdani, R.A. Akbour, Natural flocculants for the treatment of wastewaters containing dyes or heavy metals: a state-of-the-art review, J. Environ. Chem. Eng. 9 (2021), 106060, https://doi.org/10.1016/j.jece.2021.106060.

[14] O. Aly, H. Ahmed, Application of ultra-filtration technique as a water purification technology in Egypt-case study, International Research Journal of Advanced Engineering and Science 6 (2021) 174–178, https://doi.org/10.1007/s11356-020-10397-9.

[15] P.K. Pandis, C. Kalogirou, E. Kanellou, C. Vaitsis, M.G. Savvidou, G. Sourkouni, A.A. Zorpas, C. Argirusis, Key points of advanced oxidation processes (AOPs) for wastewater, organic pollutants and pharmaceutical waste treatment: a mini review, ChemEngineering 6 (2022) 8, https://doi.org/10.3390/chemengineering6010008.

[16] S. Ghosh, O. Falyouna, A. Malloum, A. Othmani, C. Bornman, H. Bedair, H. Onyeaka, Z.T. Al-Sharify, A.O. Jacob, T. Miri, A general review on the use of advance oxidation and adsorption processes for the removal of furfural from industrial effluents, Microporous Mesoporous Mater. 331 (2022), 111638, https://doi.org/10.1016/j.micromeso.2021.111638.

[17] B.M. Adesanmi, Y.-T. Hung, H.H. Paul, C.R. Huhnke, Comparison of dye wastewater treatment methods: a review, GSC Advanced Research and Reviews 10 (2022) 126–137, https://doi.org/10.30574/gscarr.2022.10.2.0054.

[18] K. Xie, J. Fang, L. Li, J. Deng, F. Chen, Progress of graphite carbon nitride with different dimensions in the photocatalytic degradation of dyes: a review, J. Alloys Compd. (2022), 163589, https://doi.org/10.1016/j.jallcom.2021.163589.

[19] J. Hong, K.-H. Cho, V. Presser, X. Su, Recent advances in wastewater treatment using semiconductor photocatalysts, Curr. Opin. Green Sustainable Chem. (2022), 100644, https://doi.org/10.1016/j.cogsc.2022.100644.

[20] P. Singh, B. Mohan, V. Madaan, R. Ranga, P. Kumari, S. Kumar, V. Bhankar, P. Kumar, K. Kumar, Nanomaterials photocatalytic activities for waste water treatment: a review, Environ. Sci. Pollut. Control Ser. 29 (2022) 69294–69326, https://doi.org/10.1007/s11356-022-22550-7.

[21] J. Chakraborty, I. Nath, F. Verpoort, A physicochemical introspection of porous organic polymer photocatalysts for wastewater treatment, Chem. Soc. Rev. 51 (2022) 1124–1138, https://doi.org/10.1039/D1CS00916H.

[22] L. Yang, D. Fan, Z. Li, Y. Cheng, X. Yang, T. Zhang, A review on the bioinspired photocatalysts and photocatalytic systems, Advanced Sustainable Systems 6 (2022), 2100477, https://doi.org/10.1002/adsu.202100477.

[23] S. Silvestri, A.R. Fajardo, B.A. Iglesias, Supported porphyrins for the photocatalytic degradation of organic contaminants in water: a review, Environ. Chem. Lett. (2022) 1–41, https://doi.org/10.1007/s10311-021-01344-2.

[24] M. Hu, H. Lou, X. Yan, X. Hu, R. Feng, M. Zhou, In-situ fabrication of ZIF-8 decorated layered double oxides for adsorption and photocatalytic degradation of methylene blue, Microporous Mesoporous Mater. 271 (2018) 68–72, https://doi.org/10.1016/j.micromeso.2018.05.048.

[25] Z.H. Jabbar, B.H. Graimed, M.A. Issa, S.H. Ammar, S.E. Ebrahim, H.J. Khadim, A.A. Okab, Photocatalytic degradation of Congo red dye using magnetic silica-coated Ag2WO4/Ag2S as Type I heterojunction photocatalyst: stability and mechanisms studies, Mater. Sci. Semicond. Process. 153 (2023), 107151, https://doi.org/10.1016/j.mssp.2022.107151.

[26] S. Fatima, S. Rizwan, Synergetic catalytic and photocatalytic performances of Tin-doped BiFeO3/graphene nanoplatelet hybrids under dark and light conditions, ACS Omega 8 (2023) 3736–3744, https://doi.org/10.1021/acsomega.2c04971.

[27] G. Zhang, A. Song, Y. Duan, S. Zheng, Enhanced photocatalytic activity of TiO2/zeolite composite for abatement of pollutants, Microporous Mesoporous Mater. 255 (2018) 61–68, https://doi.org/10.1016/j.micromeso.2017.07.028.

[28] M. Li, H. Zhao, Z.-Y. Lu, Porphyrin-based porous organic polymer, Py-POP, as a multifunctional platform for efficient selective adsorption and photocatalytic degradation of cationic dyes, Microporous Mesoporous Mater. 292 (2020), 109774, https://doi.org/10.1016/j.micromeso.2019.109774.

[29] M. Mondal, M. Halder, S. Pradhan, Nanoplate like heterostructured BiOBr/BiBr/FeBr2 nanocomposites with enhanced photocatalytic activity for wastewater treatment by removing organic dyes: interfacial consecutive dual Z scheme electron transfer, J. Environ. Chem. Eng. 10 (2022), 107240, https://doi.org/10.1016/j.jece.2022.107240.

[30] S. Gulati, K. Goyal, A. Arora, S. Kumar, M. Trivedi, S. Jain, Bismuth ferrite (BiFeO3) perovskite-based advanced nanomaterials with state-of-the-art photocatalytic performance in water cleanup, Environmental Science: Water Research & Technology 8 (2022) 1590–1618, https://doi.org/10.1039/D2EW00027J.

[31] V. Subhiksha, S. Kokilavani, S.S. Khan, Recent advances in degradation of organic pollutant in aqueous solutions using bismuth based photocatalysts: a review, Chemosphere 290 (2022), 133228, https://doi.org/10.1016/j.chemosphere.2021.133228.

[32] N.M. Al-Enazi, Optimized synthesis of mono and bimetallic nanoparticles mediated by unicellular algal (diatom) and its efficiency to degrade azo dyes for wastewater treatment, Chemosphere 303 (2022), 135068, https://doi.org/10.1016/j.chemosphere.2022.135068.

[33] H. Sun, S.-Y. Lee, S.-J. Park, Bimetallic CuPd alloy nanoparticles decorated ZnO nanosheets with enhanced photocatalytic degradation of methyl orange dye, J. Colloid Interface Sci. 629 (2023) 87–96, https://doi.org/10.1016/j.jcis.2022.09.054.

[34] A. Mekki, A. Mokhtar, M. Hachemaoui, M. Beldjilali, M. fethia Meliani, H.H. Zahmani, S. Hacini, B. Boukoussa, Fe and Ni nanoparticles-loaded zeolites as effective catalysts for catalytic reduction of organic pollutants, Microporous Mesoporous Mater. 310 (2021), 110597, https://doi.org/10.1016/j.micromeso.2020.110597.

[35] H. Khan, I.H. Lone, S.E. Lofland, K.V. Ramanujachary, T. Ahmad, Exploiting multiferroicity of TbFeO3 nanoparticles for hydrogen generation through photo/electro/photoelectro-catalytic water splitting, Int. J. Hydrogen Energy 48 (2023) 5493–5505, https://doi.org/10.1016/j.ijhydene.2022.11.143.

[36] M.A. Wahba, W. Sharmoukh, S.M. Yakout, M.S. Khalil, Fast and full spectrum sunlight photocatalysts: Fe/Co or Ni implanted multiferroic LaMnO3, Opt. Mater. 124 (2022), 111973, https://doi.org/10.1016/j.optmat.2022.111973.

[37] I.H. Lone, H. Khan, A.K. Jain, J. Ahmed, K.V. Ramanujachary, T. Ahmad, Metal–organic precursor synthesis, structural characterization, and multiferroic properties of GdFeO3 nanoparticles, ACS Omega 7 (2022) 33908–33915, https://doi.org/10.1021/acsomega.2c02809.

[38] K. Mathankumar, M. Sukumar, C.S. Dash, M. Sundararajan, M. Ubaidullah, A.M. Al-Enizi, A. Sutha, M. Kausar Raza, J. Arockia Dhanraj, D. Kumar, Facile synthesis, characterization, catalytic and photocatalytic activity of multiferroic BiFeO3 perovskite nanoparticles, J. Inorg. Organomet. Polym. Mater. 32 (2022) 3476–3487, https://doi.org/10.1007/s10904-022-02382-1.

[39] G. Gupta, S.K. Kansal, A. Umar, S. Akbar, Visible-light driven excellent photocatalytic degradation of ofloxacin antibiotic using BiFeO3 nanoparticles, Chemosphere 314 (2023), 137611, https://doi.org/10.1016/j.chemosphere.2022.137611.

[40] G. Liu, Y. Lin, S. Li, C. Shi, D. Zhang, Mechanism and efficiency of photocatalytic triclosan degradation by TiO2/BiFeO3 nanomaterials, Water Sci. Technol. 86 (2022) 3133–3152, https://doi.org/10.2166/wst.2022.397.

[41] O.V. Nkwachukwu, C. Muzenda, B.A. Koiki, O.A. Arotiba, Perovskites in photoelectrocatalytic water treatment: bismuth ferrite-graphite nanoparticles composite photoanode for the removal of ciprofloxacin in water, J. Photochem. Photobiol. Chem. 434 (2023), 114275, https://doi.org/10.1016/j.jphotochem.2022.114275.

[42] M. Benyoussef, S. Saitzek, N.S. Rajput, M. Courty, M. El Marssi, M. Jouiad, Experimental and theoretical investigations of low-dimensional BiFeO3 system for photocatalytic applications, Catalysts 12 (2022) 215, https://doi.org/10.3390/catal12020215.

[43] B. Harikumar, M.K. Okla, I.A. Alaraidh, A. Mohebaldin, W. Soufan, M.A. Abdel-Maksoud, M. Aufy, A.M. Thomas, L.L. Raju, S.S. Khan, Robust visible light active CoNiO2–BiFeO3–NiS ternary nanocomposite for photo-fenton degradation of rhodamine B and methyl orange: kinetics, degradation pathway and toxicity assessment, J. Environ. Manag. 317 (2022), 115321, https://doi.org/10.1016/j.jenvman.2022.115321.

[44] E.B. Şīmşek, Z. Balta, Investigation of synergetic effect of adsorption and photocatalysis for the removal of tetracycline by BiFeO3 immobilized on copolymer seeds, Environmental Research and Technology 5 (2022) 128–136, https://doi.org/10.35208/ert.1018193.
[45] S. Ruby, D.R. Rosaline, S. Inbanathan, K. Anand, G. Kavitha, R. Srinivasan, A. Umar, H. Hegazy, H. Algarni, Sunlight-driven photocatalytic degradation of methyl orange based on bismuth ferrite (BiFeO3) heterostructures composed of interconnected nanosheets, Journal of nanoscience and nanotechnology 20 (2020) 1851–1858, https://doi.org/10.1166/jnn.2020.17174.
[46] S. Kapoor, A. Goyal, S. Bansal, S. Singhal, Emergence of bismuth substituted cobalt ferrite nanostructures as versatile candidates for the enhanced oxidative degradation of hazardous organic dyes, New J. Chem. 42 (2018) 14965–14977, https://doi.org/10.1039/C8NJ00977E.
[47] A. Afzal, M. Umair, G. Dastgeer, M. Rizwan, M. Yaqoob, R. Rashid, H. Munir, Effect of O-vacancies on magnetic properties of bismuth ferrite nanoparticles by solution evaporation method, J. Magn. Magn Mater. 399 (2016) 77–80, https://doi.org/10.1016/j.jmmm.2015.09.062.
[48] T. Wang, B. Tian, B. Han, D. Ma, M. Sun, A. Hanif, D. Xia, J. Shang, Recent advances on porous materials for synergetic adsorption and photocatalysis, Energy & Environmental Materials 5 (2022) 711–730, https://doi.org/10.1002/eem2.12229.
[49] N.S. Inchaurrondo, J. Font, Clay, Zeolite and oxide minerals: natural catalytic materials for the ozonation of organic pollutants, Molecules 27 (2022) 2151, https://doi.org/10.3390/molecules27072151.
[50] M. Mariana, A.K. Hps, E.B. Yahya, N. Olaiya, T. Alfatah, A. Suriani, A. Mohamed, Recent trends and future prospects of nanostructured aerogels in water treatment applications, J. Water Proc. Eng. 45 (2022), 102481, https://doi.org/10.1016/j.jwpe.2021.102481.
[51] S.G. Akpe, I. Ahmed, P. Puthiaraj, K. Yu, W.-S. Ahn, Microporous organic polymers for efficient removal of sulfamethoxazole from aqueous solutions, Microporous Mesoporous Mater. 296 (2020), 109979, https://doi.org/10.1016/j.micromeso.2019.109979.
[52] S. Kitagawa, Metal–organic frameworks (MOFs), Chem. Soc. Rev. 43 (2014) 5415–5418, https://doi.org/10.1039/C4CS90059F.
[53] W. Gong, Z. Chen, J. Dong, Y. Liu, Y. Cui, Chiral metal–organic frameworks, Chem. Rev. 122 (2022) 9078–9144, https://doi.org/10.1021/acs.chemrev.1c00740.
[54] Z. Wang, L. Liu, Z. Li, N. Goyal, T. Du, J. He, G.K. Li, Shaping of metal–organic frameworks: a review, Energy & Fuels 36 (2022) 2927–2944, https://doi.org/10.1021/acs.energyfuels.1c03426.
[55] M. Ma, X. Lu, Y. Guo, L. Wang, X. Liang, Combination of metal-organic frameworks (MOFs) and covalent organic frameworks (COFs): recent advances in synthesis and analytical applications of MOF/COF composites, TrAC, Trends Anal. Chem. (2022), 116741, https://doi.org/10.1016/j.trac.2022.116741.
[56] R. Freund, O. Zaremba, G. Arnauts, R. Ameloot, G. Skorupskii, M. Dincă, A. Bavykina, J. Gascon, A. Ejsmont, J. Goscianska, The current status of MOF and COF applications, Angew. Chem. Int. Ed. 60 (2021) 23975–24001, https://doi.org/10.1002/anie.202106259.
[57] J. Annamalai, P. Murugan, D. Ganapathy, D. Nallaswamy, R. Atchudan, S. Arya, A. Khosla, S. Barathi, A.K. Sundramoorthy, Synthesis of various dimensional metal organic frameworks (MOFs) and their hybrid composites for emerging applications–a review, Chemosphere (2022), 134184, https://doi.org/10.1016/j.chemosphere.2022.134184.
[58] Y. Peng, T. Zhou, J. Ma, Y. Bai, S. Cao, H. Pang, Metal-organic framework (MOF) composites as promising materials for energy storage applications, Adv. Colloid Interface Sci. (2022), 102732, https://doi.org/10.1016/j.cis.2022.102732.
[59] N. Rabiee, M. Atarod, M. Tavakolizadeh, S. Asgari, M. Rezaei, O. Akhavan, A. Pourjavadi, M. Jouyandeh, E.C. Lima, A.H. Mashhadzadeh, Green metal-organic frameworks (MOFs) for biomedical applications, Microporous Mesoporous Mater. (2022), 111670, https://doi.org/10.1016/j.micromeso.2021.111670.
[60] S.H. Goh, H.S. Lau, W.F. Yong, Metal–organic frameworks (MOFs)-based mixed matrix membranes (MMMs) for gas separation: a review on advanced materials in harsh environmental applications, Small 18 (2022), 2107536, https://doi.org/10.1002/smll.202107536.
[61] Q. Wang, Q. Gao, A.M. Al-Enizi, A. Nafady, S. Ma, Recent advances in MOF-based photocatalysis: environmental remediation under visible light, Inorg. Chem. Front. 7 (2020) 300–339, https://doi.org/10.1039/C9QI01120J.
[62] J. Aguilera-Sigalat, D. Bradshaw, Synthesis and applications of metal-organic framework–quantum dot (QD@ MOF) composites, Coord. Chem. Rev. 307 (2016) 267–291, https://doi.org/10.1016/j.ccr.2015.08.004.
[63] Y. Xiao, C. Chen, Y. Wu, J. Wang, Y. Yin, J. Chen, X. Huang, P. Qi, B. Zheng, Water-stable Al-TCPP MOF nanosheets with hierarchical porous structure for removal of chlorantraniliprole in water, Microporous Mesoporous Mater. 324 (2021), 111272, https://doi.org/10.1016/j.micromeso.2021.111272.
[64] F. Yang, M. Du, K. Yin, Z. Qiu, J. Zhao, C. Liu, G. Zhang, Y. Gao, H. Pang, Applications of metal-organic frameworks in water treatment: a review, Small 18 (2022), 2105715, https://doi.org/10.1002/smll.202105715.
[65] M. Beydaghdari, F. Hooriabad Saboor, A. Babapoor, V.V. Karve, M. Asgari, Recent advances in MOF-based adsorbents for dye removal from the aquatic environment, Energies 15 (2022) 2023, https://doi.org/10.3390/en15062023.
[66] Z.-h. Yang, J. Cao, Y.-p. Chen, X. Li, W.-p. Xiong, Y.-y. Zhou, C.-y. Zhou, R. Xu, Y.-r. Zhang, Mn-doped zirconium metal-organic framework as an effective adsorbent for removal of tetracycline and Cr (VI) from aqueous solution, Microporous Mesoporous Mater. 277 (2019) 277–285, https://doi.org/10.1016/j.ijhydene.2022.11.143.
[67] B. Chen, Y. Li, M. Li, M. Cui, W. Xu, L. Li, Y. Sun, M. Wang, Y. Zhang, K. Chen, Rapid adsorption of tetracycline in aqueous solution by using MOF-525/graphene oxide composite, Microporous Mesoporous Mater. 328 (2021), 111457, https://doi.org/10.1016/j.micromeso.2021.111457.
[68] G. Sriram, A. Bendre, E. Mariappan, T. Altalhi, M. Kigga, Y.C. Ching, H.-Y. Jung, B. Bhaduri, M. Kurkuri, Recent trends in the application of metal-organic frameworks (MOFs) for the removal of toxic dyes and their removal mechanism-a review, Sustainable Materials and Technologies 31 (2022), e00378, https://doi.org/10.1016/j.susmat.2021.e00378.
[69] I.M. El-Sewify, A. Radwan, A. Shahat, M. El-Shahat, M.M. Khalil, Superior adsorption and removal of aquaculture and bio-staining dye from industrial wastewater using microporous nanocubic Zn-MOFs, Microporous Mesoporous Mater. 329 (2022), 111506, https://doi.org/10.1016/j.micromeso.2021.111506.
[70] X. Zhang, J. Wang, X.-X. Dong, Y.-K. Lv, Functionalized metal-organic frameworks for photocatalytic degradation of organic pollutants in environment, Chemosphere 242 (2020), 125144, https://doi.org/10.1016/j.chemosphere.2019.125144.
[71] X. Wang, W. Mao, J. Zhang, Y. Han, C. Quan, Q. Zhang, T. Yang, J. Yang, X.a. Li, W. Huang, Facile fabrication of highly efficient g-C_3N_4/$BiFeO_3$ nanocomposites with enhanced visible light photocatalytic activities, J. Colloid Interface Sci. 448 (2015) 17–23, https://doi.org/10.1016/j.jcis.2015.01.090.
[72] O.P. Bajpai, S. Mandal, R. Ananthakrishnan, P. Mandal, D. Khastgir, S. Chattopadhyay, Structural features, magnetic properties and photocatalytic activity of bismuth ferrite nanoparticles grafted on graphene nanosheets, New J. Chem. 42 (2018) 10712–10723, https://doi.org/10.1039/C8NJ02030B.
[73] F. Noori, A. Gholizadeh, Structural, optical, magnetic properties and visible light photocatalytic activity of $BiFeO_3$/graphene oxide nanocomposites, Mater. Res. Express 6 (2020) 1250g1, https://doi.org/10.1088/2053-1591/ab6807, 10.1088/2053-1591/ab6807.
[74] R. Skiker, M. Zouraibi, M. Saidi, K. Ziat, Facile coprecipitation synthesis of novel $Bi1_2TiO_20$/$BiFeO_3$ heterostructure serie with enhanced photocatalytic activity for removal of methyl orange from water, J. Phys. Chem. Solid. 119 (2018) 265–275, https://doi.org/10.1016/j.jpcs.2018.04.010.
[75] B. Samran, S. Chaiwichian, Highly enhanced photoactivity of $BiFeO_3$/Bi_2WO_6 composite films under visible light irradiation, Phys. B Condens. Matter 575 (2019), 411683, https://doi.org/10.1016/j.physb.2019.411683.
[76] E. Moradi, H. Farajnejad Ghadi, M. Rabbani, R. Rahimi, Microwave-assisted synthesized and characterization of $BiFeO_3$ (CTAB/PEG/PVA) nanocomposites by the auto-combustion method with efficient visible-light photocatalytic dye degradation, J. Mater. Sci. Mater. Electron. 32 (2021) 8237–8248, https://doi.org/10.1007/s10854-020-05202-9.
[77] G.D. Smith, J.M. Esson, V.J. Chen, R.M. Hanson, Forensic dye analysis in cultural heritage: unraveling the authenticity of the earliest Persian knotted-pile silk carpet Forensic Science, International: Synergy 3 (2021), 100130, https://doi.org/10.1016/j.fsisyn.2020.11.004.
[78] Y. Ding, C. Sun, X. Xu, Simultaneous identification of nine carcinogenic dyes from textiles by liquid chromatography/electrospray ionization mass spectrometry via negative/positive ion switching mode, Eur. J. Mass Spectrom. 15 (2009), 705e713, https://doi.org/10.1255/ejms.1032.
[79] H.N. Abdelhamid, Surfactant assisted synthesis of hierarchical porous metal-organic frameworks nanosheets, Nanotechnology 30 (2019), 435601, https://doi.org/10.1088/1361-6528/ab30f6.
[80] A.A. Kassem, H.N. Abdelhamid, D.M. Fouad, S.A. I brahim, Catalytic reduction of 4-nitrophenol using copper terephthalate frameworks and CuO@ C composite, J. Environ. Chem. Eng. 9 (2021), 104401, https://doi.org/10.1016/j.jece.2020.104401.